Experimental Observation of a Topological Band Gap Opening in Ultracold Fermi Gases with Two-Dimensional Spin-Orbit Coupling

Zengming Meng,[1,2] Lianghui Huang,[1,2] Peng Peng,[1] Donghao Li,[1] Liangchao Chen,[1] Yong Xu,[3] Chuanwei Zhang,[3] Pengjun Wang,[1,2] and Jing Zhang[1,4,*]

[1]*State Key Laboratory of Quantum Optics and Quantum Optics Devices, Institute of Opto-Electronics, Shanxi University, Taiyuan 030006, People's Republic of China*

[2]*Collaborative Innovation Center of Extreme Optics, Shanxi University, Taiyuan 030006, People's Republic of China*

[3]*Department of Physics, The University of Texas at Dallas, Richardson, Texas 75080-3021, USA*

[4]*Synergetic Innovation Center of Quantum Information and Quantum Physics, University of Science and Technology of China, Hefei, Anhui 230026, People's Republic of China*

(Received 21 February 2016; revised manuscript received 26 September 2016; published 2 December 2016)

The recent experimental realization of synthetic spin-orbit coupling (SOC) opens a new avenue for exploring novel quantum states with ultracold atoms. However, in experiments for generating two-dimensional SOC (e.g., Rashba type), a perpendicular Zeeman field, which opens a band gap at the Dirac point and induces many topological phenomena, is still lacking. Here, we theoretically propose and experimentally realize a simple scheme for generating two-dimensional SOC and a perpendicular Zeeman field simultaneously in ultracold Fermi gases by tuning the polarization of three Raman lasers that couple three hyperfine ground states of atoms. The resulting band gap opening at the Dirac point is probed using spin injection radio-frequency spectroscopy. Our observation may pave the way for exploring topological transport and topological superfluids with exotic Majorana and Weyl fermion excitations in ultracold atoms.

DOI: 10.1103/PhysRevLett.117.235304

Spin-orbit coupling (SOC), the intrinsic interaction between a particle spin and its motion, plays a key role in many important phenomena, ranging from anomalous Hall effects [1] to topological insulators and superconductors [2–4]. Although SOC is ubiquitous in nature, the experimental control and observation of SOC induced effects are quite difficult. In this context, the recent experimental realization of synthetic SOC for cold atoms [5–12] provides a completely new and tunable platform for exploring SOC related physics. Early experiments only realized the 1D SOC (i.e., an equal sum of Rashba and Dresselhaus coupling, $\propto k_x\sigma_y$) using two counterpropagating Raman lasers [5–12]. Many theoretical proposals have explored the generation of 2D SOC (i.e., $\propto \alpha k_x\sigma_y + \beta k_y\sigma_x$) [13–20] as well as their interesting physical properties in Bose and Fermi gases [21–26]. Recently, 2D SOC was also experimentally realized in ultracold ^{40}K Fermi gases [27], using three Raman lasers and the associated stable Dirac point on a 2D momentum plane was observed [27].

The experimental generation of SOC is usually accompanied with a Zeeman field, which breaks various symmetries of the underlying system and induces interesting quantum phenomena. The accompanied Zeeman field can be in-plane (e.g., $V\sigma_y$ for SOC $\propto k_x\sigma_y$) or perpendicular (e.g., $V\sigma_z$ for SOC $\propto \alpha k_x\sigma_y + \beta k_y\sigma_x$). The in-plane Zeeman field, while preserving the Dirac point, makes the band dispersion asymmetric, leading to new quantum states such as Fulde-Ferrell superfluids [28–31]. In contrast, the perpendicular Zeeman field can open a topological band gap at the Dirac point of the SOC, leading to many interesting topological transport [1] and superfluid phenomena, such as the long-sought Majorana [32,33] and Weyl [24,34,35] fermions. In cold atom experiments, although both in-plane and perpendicular Zeeman fields have been realized with 1D SOC, only the in-plane Zeeman field was realized with 2D SOC [27]. A perpendicular Zeeman field with 2D SOC is still lacking but highly desired in experiments for the observation of various topological transport and superfluid phenomena.

In this Letter, we theoretically propose and experimentally realize a simple scheme for generating 2D SOC and a perpendicular Zeeman field simultaneously. The same setup for generating 2D SOC in previous work [27] is used, in which three far-detuned Raman lasers couple three hyperfine ground states. We only change the polarization of the Raman lasers, which can create the perpendicular Zeeman field and open the band gap at the Dirac point. This scheme significantly simplifies the experimental requirement compared with existing theoretical proposals [36,37], which need additional laser beams, complicated optical configuration, and controllable relative laser phases to create the perpendicular Zeeman field. We observe and characterize the topological band gap opening induced by the perpendicular Zeeman field using spin injection radio-frequency (rf) spectroscopy, which are in good agreement with our theoretical calculations.

Experimental setup and theoretical modeling.—The experimental setup as well as theoretical modeling for generating and observing 2D SOC have been described in detail in our previous work [27]. In this section we briefly describe our experimental system and the corresponding theoretical modeling with more details provided in the Supplemental Material [38]. We point out that the lack of complex Raman coupling strength is responsible for the lack of a perpendicular Zeeman field and the resulting topological band gap opening in our previous work [27].

Specifically, we consider ultracold ^{40}K Fermi gases with three relevant hyperfine states within the $4^2S_{1/2}$ ground electronic manifold, $|1\rangle = |F = 9/2, m_F = 3/2\rangle$, $|2\rangle = |F = 9/2, m_F = 1/2\rangle$, and $|3\rangle = |F = 7/2, m_F = 1/2\rangle$, where (F, m_F) are the quantum numbers for hyperfine ground states as shown in Fig. 1(a). A homogeneous bias magnetic field $B_0 = 121.4$ G along the z axis (the gravity direction) produces a Zeeman shift to isolate these three hyperfine states from others in the Raman transitions, as shown in Fig. 1(a). We can neglect other hyperfine states and treat this system as one with three ground states. Three far-detuned Raman lasers propagating on the xy plane couple these three ground states to the electronically excited states [Fig. 1(b)].

For the far-detuned lasers, the excited states can be adiabatically eliminated, and the Hamiltonian is written as $H = p_z^2/(2m) + H_{xy}$ with [27]

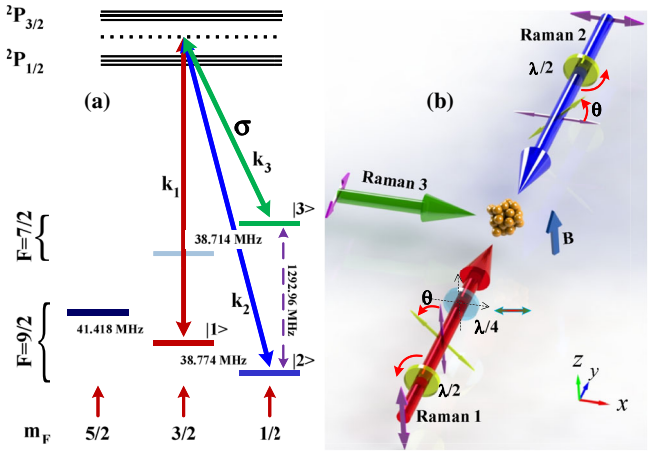

FIG. 1. Scheme of the atom-light interaction configuration for generating 2D synthetic SOC and an effective perpendicular Zeeman field simultaneously. (a) Schematic of energy levels of ^{40}K and Raman transitions. Each of the three Raman lasers dresses one hyperfine ground state. (b) The experimental geometry and laser configuration. The Raman lasers 1-3 are initially prepared with the linear polarization along the z, x, and y directions, respectively. Then the Raman lasers 1 and 2 pass through a $\lambda/2$ wave plate, which rotates their linear polarizations by the same angle θ synchronously. Cases I and II correspond to without and with the $\lambda/4$ wave plate after the $\lambda/2$ wave plate for the Raman laser 1.

$$H_{xy} = \sum_{j=1}^{3}\left(\frac{(\mathbf{p}-\mathbf{k}_j)^2}{2m} + \delta_j\right)|j\rangle\langle j| - \sum_{j'\neq j}\frac{\Omega_{jj'}}{2}|j\rangle\langle j'|, \quad (1)$$

under the hyperfine ground state basis $\{|j\rangle, j = 1, 2, 3\}$. Here, $\mathbf{p} = p_x\mathbf{e}_x + p_y\mathbf{e}_y$ denotes the momentum of atoms in the xy plane, δ_1 is set as zero (energy reference) for simplification, and δ_2 (δ_3) corresponds to the two-photon Raman detuning between Raman lasers 1 and 2 (1 and 3). $\mathbf{k}_1 = k_r\mathbf{e}_y$, $\mathbf{k}_2 = -k_r\mathbf{e}_y$, and $\mathbf{k}_3 = k_r\mathbf{e}_x$ are the photon momenta of three Raman lasers with the single-photon recoil momentum $k_r = 2\pi\hbar/\lambda$. Three $\Omega_{jj'} = \Omega_{j'j}^*$ describe the Raman coupling strength between hyperfine ground states $|j\rangle \leftrightarrow |j'\rangle$ through Raman lasers. k_r and recoil energy $E_r = k_r^2/2m$ are taken as natural momentum and energy units.

The origin of 2D SOC in this system can be understood from the eigenstates of the atom-laser interaction part (the nondiagonal terms $\Omega_{jj'}$) of the Hamiltonian (1), which contain two degenerate dark states and one bright state separated by an energy gap [38]. Denote two degenerate dark states as the pseudospin states, the 3×3 Hamiltonian (1) can be projected to the dark state subspace, leading to an effective spin-half Hamiltonian with 2D SOC and effective Zeeman fields. In previous experiments [27] as well as existing theoretical proposals, $\Omega_{jj'}$ are chosen to be real numbers [39], yielding

$$H_{\text{eff}} = \mathbf{p}^2/2m + H_{\text{SOC}} + V_I, \quad (2)$$

where the 2D SOC $H_{\text{SOC}} = -\alpha p_y\sigma_x + (\beta_x p_x - \beta_y p_y)\sigma_y$ and the in-plane Zeeman field $V_I = V_x\sigma_x + V_y\sigma_y$ in the xy plane. α, β_x, β_y, V_x, and V_y are parameters determined by the experimental parameters $\mathbf{k}_j$, δ_j, and $\Omega_{jj'}$. Pauli matrices σ_i are defined on the dark state pseudospin basis. The in-plane Zeeman field V_I shifts the Dirac cone at $\mathbf{p} = \mathbf{0}$ to another position in the momentum space, but cannot open a band gap at the Dirac point. Such a controlled shift of the Dirac point has been observed in our experiment [27]. However, the opening of a topological band gap at the Dirac point requires a perpendicular Zeeman field of the form $V_z\sigma_z$, which demands the generation of complex Raman coupling $\Omega_{jj'}$ in experiments.

Realization of a perpendicular Zeeman field.—Because the Raman coupling strengths $\Omega_{jj'}$ are proportional to $\vec{E}_j \times \vec{E}_{j'}$, the generation of complex $\Omega_{jj'}$ requires the tuning of the polarizations of Raman lasers from linear to elliptical, which can be realized in experiments using $\lambda/2$ and $\lambda/4$ wave plates.

The scheme for inserting $\lambda/2$ and $\lambda/4$ wave plates in the experimental setup is shown in Fig. 1(b). Here two $\lambda/2$ wave plates rotate the polarizations of Raman lasers 1 and 2 by an angle θ, yielding $\vec{E}_1 = A_1(\cos\theta\hat{\mathbf{e}}_\parallel + \sin\theta\hat{\mathbf{e}}_\perp)$ (without the $\lambda/4$ wave plate) and $\vec{E}_2 = A_2(\cos\theta\hat{\mathbf{e}}_\perp + \sin\theta\hat{\mathbf{e}}_\parallel)$,

where $\hat{\mathbf{e}}_\perp$ and $\hat{\mathbf{e}}_\parallel$ components correspond to σ and π polarizations with respect to the quantization axis $\mathbf{z}$ defined by the magnetic field. The rotation still keeps $\vec{E}_1$ and $\vec{E}_2$ orthogonal. The additional $\lambda/4$ wave plate can change $\vec{E}_1$ to elliptical polarization $\vec{E}_1 = A_1(\cos\theta\hat{\mathbf{e}}_\parallel + i\sin\theta\hat{\mathbf{e}}_\perp)$, where the imaginary part is responsible for generating complex Ω_{12}. To illustrate this, we consider two different cases (I) without and (II) with the $\lambda/4$ wave plate. Hereafter, we denote $\Omega_{jj'}$ as the Raman coupling strength before the $\lambda/2$ and $\lambda/4$ wave plates. Careful analysis of the Raman transition selection rules (note that $\vec{E}_3 = A_3\hat{\mathbf{e}}_\perp$) shows [38].

Case I.—$\Omega^I_{23} = \cos\theta\Omega_{23}$, $\Omega^I_{13} = \cos\theta\Omega_{13}$, and $\Omega^I_{12} = \Omega_{12}$. The rotations induced by the $\lambda/2$ wave plates keep $\Omega^I_{jj'}$ real, and therefore only shift the Dirac point position and cannot open a band gap [see Fig. 2(a1)].

Case II.—$\Omega^{II}_{13} = \cos\theta\Omega_{13}$, $\Omega^{II}_{23} = \cos\theta\Omega_{23}$, and $\Omega^{II}_{12} = \Omega_{12}(\cos^2\theta + i\sin^2\theta)$, yielding an imaginary part $H_Z = -i(\Omega_{12}\sin^2\theta/2)|1\rangle\langle 2| + \text{H.c.}$ in the Hamiltonian (1), which cannot be gauged out by varying the phase of the wave function for each hyperfine ground state. This term opens a band gap at the Dirac point as shown in Fig. 2(b1). In the degenerate dark state pseudospin basis, this term gives $V_z\sigma_z$, the perpendicular Zeeman field. The energy gap at the Dirac point can be controlled precisely by adjusting the rotation angle θ. Note H_Z has the same form as that in a previous theoretical proposal [37] that requires complicated setup of additional lasers. Our scheme is much simpler and more robust because it only need tune the polarizations of three Raman lasers.

The change of $\Omega^i_{jj'}$ induced by the wave plates can be measured using the Rabi oscillation between two hyperfine ground states [10,38]. We obtain Ω^i_{12} for cases I and II, respectively, as the function of the rotation angle θ as shown in Fig. 3(a). For case I, Ω^I_{12} keeps unchanged for different θ. In case II, we measure the absolute value of Ω^{II}_{12} because Ω^{II}_{12} is a complex number, which shows $\sqrt{\cos^4\theta + \sin^4\theta}$ dependence for different θ [Fig. 3(a)], agreeing with the theory. The measurements for Ω^i_{13} and Ω^i_{23} also demonstrate their $\cos\theta$ dependence [Fig. 3(b)].

Observation of band gap opening.—The imaginary part $i\Omega_{12}\sin^2\theta$ of Ω^{II}_{12} opens a band gap at the Dirac point of the energy-momentum dispersions, corresponding to a perpendicular Zeeman field. Such a topological band gap opening can be measured by spin injection rf spectroscopy, which uses the rf field to drive atoms from a free spin-polarized state into an empty 2D SOC system [27].

In our experiment, a degenerate Fermi gas ^{40}K of 2×10^6 is prepared at the free reservoir hyperfine state $|9/2, 5/2\rangle$ in a crossed optical dipole trap. We ramp the homogeneous bias magnetic field to the value $B_0 = 121.4$ G, and then apply three Raman lasers with the wavelength 768.85 nm in 60 ms from zero to its final value. Subsequently, a Gaussian shape pulse of the rf field is applied for 450 μs to drive atoms from the initial $|9/2, 5/2\rangle$ state to the final empty state with 2D SOC. Since the rf field does not transfer momentum to the atoms, spin injection occurs when the frequency of the rf matches the energy difference between the initial and final states [38]. At last, the Raman lasers, the optical trap, and the bias magnetic field are switched off abruptly, and atoms freely expand for 12 ms with a magnetic field gradient applied along the x axis. The absorption image is taken along the z direction. We use a Gaussian fit to locate the maximum of the measured atomic density as a function of the momentum and the rf frequency

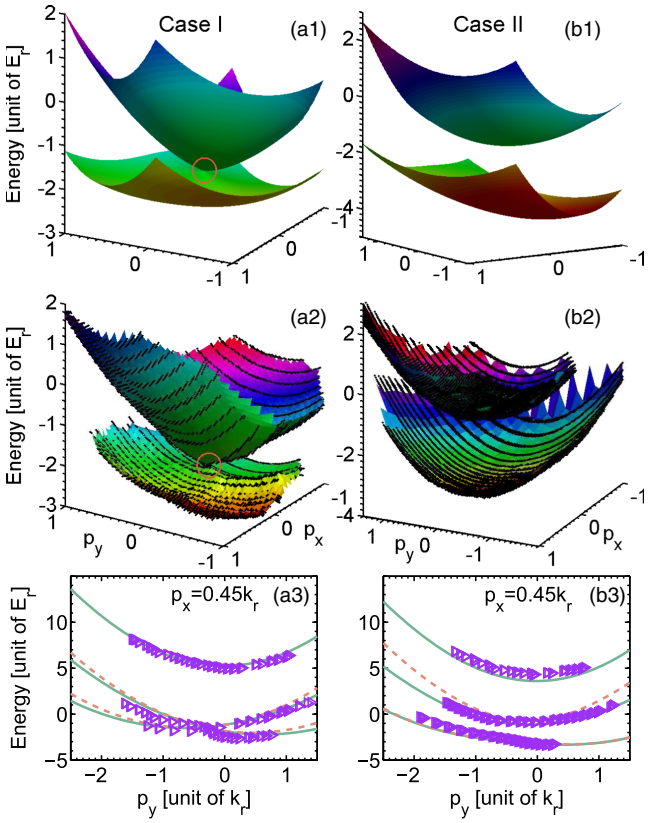

FIG. 2. The energy dispersions of dressed atoms measured by rf spin-injection spectroscopy. Columns (a1)–(a3) and (b1)–(b3) correspond to the energy-momentum dispersions of 2D SOC without (case I) and with (case II) effective perpendicular Zeeman field, respectively. The experimental parameters are $\Omega_{12} = -4.97E_r$, $\Omega_{13} = 5.46E_r$, $\Omega_{23} = 6.46E_r$, $\delta_2 = -0.5E_r$, $\delta_3 = -1.8E_r$ and $\theta = 45°$. (a1) and (b1) are theoretical results calculated using the Hamiltonian (1) with the experimental parameters. (a2) and (b2) are experimental results measured by rf spin-injection spectroscopy. The black dots represent the experimental data. The yellow circles in (a1) and (a2) indicate the Dirac points. In both rows, we only show the lowest two bands for better visualization of the Dirac points and the band gap opening. (a3) The cross-section drawings of (a1) and (a2) in the energy-p_y coordinates for $p_x = 0.45k_r$. Triangles are from experimental data. Solid and dashed lines are from theoretical calculations using the full [Eq. (1)] and effective [Eq. (2)] Hamiltonians, respectively. (b3) The cross-section drawings of (b1) and (b2).

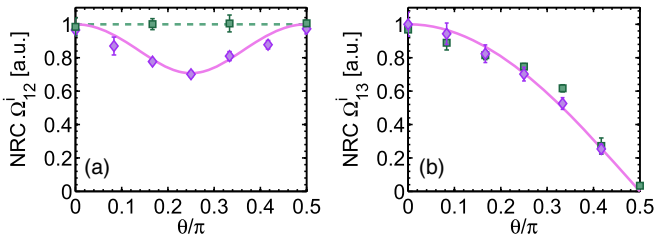

FIG. 3. Measurement of the Raman coupling strength by Rabi oscillations between two hyperfine ground states. Plot of the Raman coupling strengths Ω^i_{12} (a) and Ω^i_{13} (b) versus θ. The green squares and purple diamonds correspond to cases I and II, respectively. NRC represents normalized Raman coupling. The solid and dashed lines are theoretical curves.

from the absorption image, from which we can obtain the energy band dispersion.

Figure 2 shows the momentum-resolved spin-injection spectra for cases I and II. Other experimental parameters are the same for two cases. When the wavelength of the Raman lasers is tuned to 768.85 nm between the D_1 and D_2 lines, two lower-energy dispersions touch at a Dirac point for case I as shown in Figs. 2(a2)–2(a3), which demonstrate the 2D SOC [27]. With the $\lambda/4$ wave plate (case II), the energy gap at the Dirac point is opened, as shown in Figs. 2(b2)–2(b3). We perform numerical calculations for the energy spectra of the Hamiltonian (1) and the effective Hamiltonian (2) with corresponding experimental parameters, which show good agreement with the experimental data. Note that the eigenenergy of the effective Hamiltonian (2) deviates from the exact Hamiltonian (1) for momentum away from the Dirac points.

In experiments, we determine the band gap and the position of the Dirac point by searching the minimum of the energy differences between the lowest two bands in experiments, as shown in Figs. 4(a), 4(b) for two cases with $\theta = \pi/4$. The stars and dots represent the positions of band gap minima measured in experiments and obtained in theory using the exact 3×3 Hamiltonian (1) [38], respectively. The band gap is very large for a large $\theta = \pi/4$; therefore, the bands are very flat around the gap minima, yielding large uncertainty for the measurement of Dirac point positions in experiments [see the dashed line box in Fig. 4(b)].

Figures 4(c), 4(d) show the band gap and Dirac point positions as a function of θ. We see the band gap increases with the angle θ, while the positions of the Dirac points only change slightly, demonstrating the tunability of the topological band gaps through varying the polarization of the Raman laser. The measured single particle band gaps and Dirac point position do not exactly agree with theoretical calculations from the Hamiltonians (1) and (2), which may be attributed to, for instance, the finite energy resolution of rf spectrum and the corresponding finite momentum width, the uncertainty in the Gaussian fit process to locate the maximum of the measured atomic

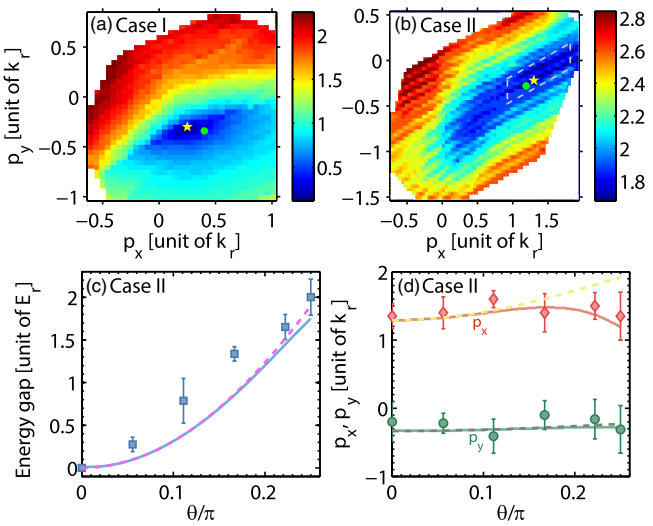

FIG. 4. Tunable band gap at the Dirac point induced by the perpendicular Zeeman field. (a),(b) Plot of the energy differences between the lowest two bands in experiments. The stars and dots correspond to the Dirac point positions in experiments and theory, respectively. (c),(d) The band gap (c) and the position of the Dirac point (d) are plotted as the function of θ. In both figures, the squares and diamonds represent experimental data. The solid and dashed lines represent theoretical calculations using the 3×3 Hamiltonian (1) and the spin-half effective Hamiltonian (2), respectively. The experimental parameters are the same as Fig. 2.

density that determines the atom momentum, and the stability of the magnetic field, etc.

Discussion.—The topological properties of the induced band gap by the perpendicular Zeeman field can be characterized by the Berry curvature of each band [1] (see Supplemental Material [38] for the plot of the Berry curvatures in the lowest two bands), which is a delta function at the Dirac point for case I, but becomes nonzero for all $\mathbf{p}$ with a peak located at the Dirac point for case II. The corresponding Berry phases are found to be $\mp\,\pi$ for the lowest two bands, as expected.

By varying the Raman laser intensities in experiments, the positions of the Dirac points, the form of the 2D SOC, and the associated in-plane Zeeman field can be tuned. Together with the tunable perpendicular Zeeman field, our system provides a potential platform for exploring various SOC related transport phenomena for noninteracting atoms and superfluid physics for Cooper pairs. For instance, the coexistence of 2D SOC and perpendicular Zeeman field yields nonzero Berry curvature, leading to an anomalous velocity for atoms [1]. The resulting anomalous Hall effects may be observed in a noninteracting Fermi gas [36]. The generated perpendicular Zeeman field is at the order of recoil energy E_r, which is large enough for realizing topological superfluids [32,33] and associated Majorana and Weyl fermions [24,34,35]. The generated Zeeman field contains both in-plane and perpendicular components, which make the single particle band structure highly

asymmetric, leading to the possibility of observing the long-sought Fulde-Ferrell-Larkin-Ovchinnikov superfluid phases with finite momentum pairing [28–30]. In particular, in the two-body physics level, such a system could host a dimer bound state with finite center-of-mass mechanical momentum, which may be measured in the momentum distribution [31].

In summary, we have realized a simple scheme for generating 2D SOC and a perpendicular Zeeman field simultaneously for ultracold fermionic atoms. The topological energy gap at the Dirac point can be opened and controlled precisely by the perpendicular Zeeman field. Our study should pave the way for exploring various interesting topological and other exotic superfluid phenomena arising from the *s*-wave scattering interaction.

This research is supported by the MOST (Grant No. 2016YFA0301602), NSFC (Grant No. 11234008, 11361161002) and the program for Sanjin Scholars of Shanxi Province. Y. X. and C. Z. are supported by ARO (W911NF-12-1-0334), AFOSR (FA9550-16-1-0387), and NSF (PHY-1505496).

*To whom all correspondence should be addressed.
jzhang74@sxu.edu.cn
jzhang74@yahoo.com

[1] D. Xiao, M.-C. Chang, and Q. Niu, Berry phases effects on electronic properties, Rev. Mod. Phys. **82**, 1959 (2010).
[2] M. Z. Hasan and C. L. Kane, Topological insulators, Rev. Mod. Phys. **82**, 3045 (2010).
[3] X.-L. Qi and S.-C. Zhang, Topological insulators and superconductors, Rev. Mod. Phys. **83**, 1057 (2011).
[4] J. E. Moore, The birth of topological insulators, Nature (London) **464**, 194 (2010).
[5] Y.-J. Lin, K. Jiménez-García, and I. B. Spielman, Spin-orbit-coupled Bose-Einstein condensates, Nature (London) **471**, 83 (2011).
[6] Z. Fu, P. Wang, S. Chai, L. Huang, and J. Zhang, Bose-Einstein condensate in a light-induced vector gauge potential using the 1064 nm optical dipole trap lasers, Phys. Rev. A **84**, 043609 (2011).
[7] J.-Y. Zhang *et al.*, Collective Dipole Oscillations of a Spin-Orbit Coupled Bose-Einstein Condensate, Phys. Rev. Lett. **109**, 115301 (2012).
[8] C. Qu, C. Hamner, M. Gong, C. Zhang, and P. Engels, Observation of Zitterbewegung in a spin-orbit coupled Bose-Einstein condensate, Phys. Rev. A **88**, 021604(R) (2013).
[9] A. J. Olson, S.-J. Wang, R. J. Niffenegger, C.-H. Li, C. H. Greene, and Y. P. Chen, Tunable Laudan-Zener transitions in a spin-orbit-coupled Bose-Einstein condesate, Phys. Rev. A **90**, 013616 (2014).
[10] P. Wang, Z. Yu, Z. Fu, J. Miao, L. Huang, S. Chai, H. Zhai, and J. Zhang, Spin-Orbit Coupled Degenerate Fermi Gases, Phys. Rev. Lett. **109**, 095301 (2012).
[11] L. W. Cheuk, A. T. Sommer, Z. Hadzibabic, T. Yefsah, W. S. Bakr, and M. W. Zwierlein, Spin-Injection Spectroscopy of a Spin-Orbit Coupled Fermi Gas, Phys. Rev. Lett. **109**, 095302 (2012).
[12] R. A. Williams, M. C. Beeler, L. J. LeBlanc, and I. B. Spielman, Raman-Induced Interactions in a Single-Component Fermi Gas near an S-Wave Feshbach Resonance, Phys. Rev. Lett. **111**, 095301 (2013).
[13] R. G. Unanyan, B. W. Shore, and K. Bergmann, Laser-driven population transfer in four-level atoms: Consequences of non-Abelian geometrical adiabatic phase factors, Phys. Rev. A **59**, 2910 (1999).
[14] J. Ruseckas, G. Juzeliūnas, P. Öhberg, and M. Fleischhauer, Non-Abelian Gauge Potentials for Ultracold Atoms with Degenerate Dark States, Phys. Rev. Lett. **95**, 010404 (2005).
[15] D. L. Campbell, G. Juzeliūnas, and I. B. Spielman, Realistic Rashba and Dresselhaus spin-orbit coupling for neutral atoms, Phys. Rev. A **84**, 025602 (2011).
[16] Z. F. Xu, L. You, and M. Ueda, Atomic spin-orbit coupling synthesized with magnetic-field-gradient pulses, Phys. Rev. A **87**, 063634 (2013).
[17] B. M. Anderson, I. B. Spielman, and G. Juzeliūnas, Magnetically Generated Spin-Orbit Coupling for Ultracold Atoms, Phys. Rev. Lett. **111**, 125301 (2013).
[18] Y. Zhang, L. Mao, and C. Zhang, Mean-Field Dynamics of Spin-Orbit Coupled Bose-Einstein Condensates, Phys. Rev. Lett. **108**, 035302 (2012).
[19] X. J. Liu, K. T. Law, and T. K. Ng, Realization of 2D Spin-Orbit Interaction and Exotic Topological Orders in Cold Atoms, Phys. Rev. Lett. **112**, 086401 (2014).
[20] D. L. Campbell and I. B. Spielman, Rashba realization: Raman with RF, New J. Phys. **18**, 033035 (2016).
[21] C. Wu, I. Mondragon-Shem, and X.-F. Zhou, Unconventional Bose-Einstein condensations from spin-orbit coupling, Chin. Phys. Lett. **28**, 097102 (2011).
[22] C. Wang, C. Gao, C.-M. Jian, and H. Zhai, Spin-Orbit Coupled Spinor Bose-Einstein Condensates, Phys. Rev. Lett. **105**, 160403 (2010).
[23] T.-L. Ho and S. Zhang, Bose-Einstein Condensates with Spin-Orbit Interaction, Phys. Rev. Lett. **107**, 150403 (2011).
[24] M. Gong, S. Tewari, and C. Zhang, BCS-BEC Crossover and Topological Phase Transition in 3D Spin-Orbit Coupled Degenerate Fermi Gases, Phys. Rev. Lett. **107**, 195303 (2011).
[25] H. Hu, L. Jiang, X.-J. Liu, and H. Pu, Probing Anisotropic Superfluidity in Atomic Fermi Gases with Rashba Spin-Orbit Coupling, Phys. Rev. Lett. **107**, 195304 (2011).
[26] Z.-Q. Yu and H. Zhai, Spin-Orbit Coupled Fermi Gases Cross a Feshbach Resonance, Phys. Rev. Lett. **107**, 195305 (2011).
[27] L. Huang, Z. Meng, P. Wang, P. Peng, S.-L. Zhang, L. Chen, D. Li, Q. Zhou, and J. Zhang, Experimental realization of two-dimensional synthetic spin-orbit coupling in ultracold Fermi gases, Nat. Phys. **12**, 540 (2016).
[28] Z. Zheng, M. Gong, X. Zou, C. Zhang, and G.-C. Guo, Route to observable Fulde-Ferrell-Larkin-Ovchinnikov phases in three-dimensional spin-orbit coupled degenerate Fermi gases, Phys. Rev. A **87**, 031602(R) (2013).
[29] C. Qu, Z. Zheng, M. Gong, Y. Xu, L. Mao, X. Zou, G.-C. Guo, and C. Zhang, Topological superfluids with finite-momentum pairing and Majorana fermions, Nat. Commun. **4**, 2710 (2013).

[30] W. Zhang and W. Yi, Topological Fulde–Ferrell–Larkin–Ovchinnikov states in spin-orbit coupled Fermi gases, Nat. Commun. **4**, 2711 (2013).

[31] L. Dong, L. Jiang, H. Hu, and H. Pu, Finite-momentum dimer bound state in spin-orbit coupled Fermi gas, Phys. Rev. A **87**, 043616 (2013).

[32] C. Zhang, S. Tewari, R. M. Lutchyn, and S. Das Sarma, $p_x + ip_y$ Superfluid from s-Wave Interactions of Fermionic Cold Atoms, Phys. Rev. Lett. **101**, 160401 (2008).

[33] J. D. Sau, R. M. Lutchyn, S. Tewari, and S. Das Sarma, Generic New Platform for Topological Quantum Computation using Semiconductor Heterostructures, Phys. Rev. Lett. **104**, 040502 (2010).

[34] K. Seo, L. Han, and C. A. R. & Sá de Melo, Emergence of Majorana and Dirac Particles in Ultracold Fermions via Tunable Interactions, Spin-Orbit Effects, and Zeeman Fields, Phys. Rev. Lett. **109**, 105303 (2012).

[35] Y. Xu, R. Chu, and C. Zhang, Anisotropic Weyl Fermions from Quasiparticle Excitation Spectrum of a 3D Fulde-Ferrell Superfluid, Phys. Rev. Lett. **112**, 136402 (2014).

[36] C. Zhang, Spin-orbit coupling and perpendicular Zeeman field for fermionic cold atoms: Observation of the intrinsic anomalous Hall effect, Phys. Rev. A **82**, 021607(R) (2010).

[37] S.-L. Zhu, L.-B. Shao, Z. D. Wang, and L.-M. Duan, Probing Non-Abelian Statistics of Majorana Fermions in Ultracold Atomic Superfluid, Phys. Rev. Lett. **106**, 100404 (2011).

[38] See Supplemental Material at http://link.aps.org/supplemental/10.1103/PhysRevLett.117.235304 for the detailed theoretical calculation and experimental procedure.

[39] Note that although different constant phases can be introduced for each Raman laser, which make all $\Omega_{jj'}$ complex, such phases can be easily gauged out by absorbing the phases into the definition of each hyperfine state wave function, yielding real $\Omega_{jj'}$.